ACADEMIA ROMÂNĂ
Revue Roumaine de Chimie
http://web.icf.ro/rrch/

Rev. Roum. Chim.,
2019, *64*(8), 651-662
DOI: 10.3224/rrch.2019.64.8.02

CRYSTAL STRUCTURE AND COMPUTATIONAL STUDY OF A FLUORINE-CONTAINING THIOSEMICARBAZONE

Bhuvanendra SINGH,[a] Rajeev SINGH,[b*] Rayees Ahmad BHAT,[c] Vasundhara SINGH[d] and Dilip KUMAR[c]

[a]Department of Chemistry, ITM University, Gwalior, India
[b]Department of Chemistry, Institute of Information Technology and Management, Gwalior, India
[c]Centre of Research for Chemical Sciences, Post Graduate Department of Chemistry, SMS Govt. College, Gwalior, India
[d]Department of Chemistry, KET Polytechnic Institute, Farah, Mathura, India

Received November 13, 2017

The present study reports crystal structure and computational study of a previously unreported fluorine-containing thiosemicarbazone compound, (2E)-2-[1-(4-fluorophenyl)ethylidene]-*N*-methylhydrazine-1-carbothioamide. This study includes Hirshfeld surface analysis, tautomerism study and theoretical calculations of vibrational frequencies by post Hartree-Fock MP2 *ab initio* method. The 3D plot of Hirshfeld surfaces mapped with different properties and 2D fingerprint plot for d*norm* distance were plotted and analyzed. This molecule is theoretically investigated by quantum chemical calculations for geometry optimization, tautomeric study, and vibration frequencies. The theoretically calculated vibration frequencies were compared with the experimental IR spectroscopic data. The electron localization function plot was also presented.

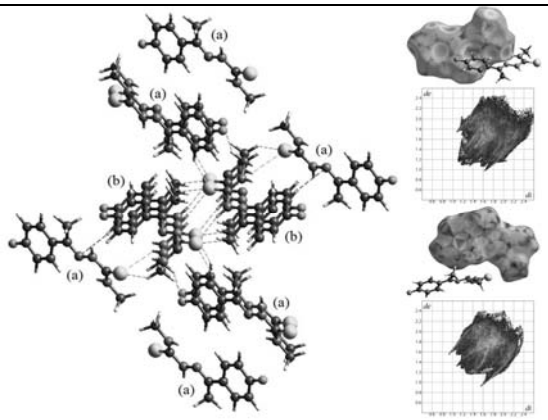

INTRODUCTION

Study of thiosemicarbazones compounds is a common research interest among researchers due to the biological properties shown by them and they are being explored extensively long back for their biological properties and pharmacological activities hoping their use as future promising drug candidates.[1–3] Thiosemicarbazones are shown to possess antibacterial activity,[4–7] antifungal activity,[8,9] antineoplastic activity,[10–24] antimalarial activity,[25] antifilarial,[26] antiviral,[17,27–35] activity. The overall activity of a molecule, in general, is an outcome of their physical molecular structure and chemical reactivity which depends more specifically on their molecular geometry, electronic structure, conformational and tautomeric behavior, hydrogen bonding capability etc. This study reports the crystal structure of (2E)-2-[1-(4-fluorophenyl)ethylidene]-*N*-methylhydrazine-1-carbothioamide (FEMHC) for the first time and it also investigates this molecule theoretically for geometry optimization, tautomerism, vibrational spectra by quantum chemical calculations and topological analysis. This study aims at the detailed investigation of the crystal and molecular structure of FEMHC. It is considered important to describe crystal and molecular structure of FEMHC. The data gathered in this study is also valuable for providing a source for comparison of theoretical predictions with experimental observations. The insight into the molecular structure of FEMHC will be valuable further as input for its pharmacological screening studies.

* Corresponding author: rajeevs_rathore@rediffmail.com; Mob: +919926244862

EXPERIMENTAL

1. Material and Instrumentation

The chemical was purchased from Sigma-Aldrich and Merck. They were used in synthesis without further purification. Single crystal X-ray diffraction was performed on Bruker Kappa Apex II CCD diffractometer. Debian 8.0 LINUX operating workstation having 2.4 GHz quad-core CPU and 32 GB RAM was used for computational investigations. ESI+ mass spectrum was recorded on an **Agilent 6520 Q-Tof** mass spectrometer. The FTIR spectrum was recorded in KBr pellets on **Perkin Elmer Spectrum II** spectrometer in the wavenumber region of 4000-400 cm^{-1} and ^1H NMR spectrum was recorded on a **Bruker AV III HD 300** MHz FT NMR spectrometer employing TMS as internal reference and $CDCl_3$ as a solvent.

2. Synthesis

FEMHC was prepared by condensation method. The ethanolic solutions of 4-methyl-3-thiosemicarbazide and 4-Fluoroacetophenone were mixed in 1:1 molar ratio. The mixture was made homogeneous by adding a little more ethanol and then refluxed on a water bath for about 1 hour. The reaction mixture was then allowed to cool overnight. The colorless crystals obtained, filtered, washed with cold ethanol, dried in air at room temperature and finally stored in a $CaCl_2$ desiccators. Colorless crystalline solid (yield = 70%; mp =261^{0}C). Single crystal of FEMHC was grown by slow evaporation over 10 days using ethyl alcohol as solvent. ESI+ HRMS m/z: 226.0873 (100%), calculated exact molecular mass – 225.0736; IR (cm^{-1}, transmittance %): 462.80 (21.68%), 590.33 (57.67%), 665.60 (56.76%), 756.33 (48.90%), 811.47 (47.89%), 839.01 (39.27%), 1045.56 (39.97%), 1106.77 (41.3%), 1160.28 (42.79%), 1230.17 (26.72%), 1299.11 (38.12%), 1367.36 (49.48%), 1413.93 (42.99%), 1495.44 (23.08%), 1549.2 (22.02%), 1602.98 (43.01%), 2939.68 (51.63%), 3304.14 (39.90%), 3370.21 (41.95%); 1H NMR (300 MHz, $CDCl_3$) δ: 2.260 (s, 3H, $-CH_3$), 3.281, 3.269 (d, 3H, $-CH_3$), 7.069–7.112 (m, 2H, aromatic), 7.667–7.703 (m, 2H, aromatic).

ESI+ HRMS technique exactly predicts $[M+H]^+$ ion peak for FEMHC. IR peak assignment is given in Table 3. The NMR peaks confirm the molecular structure of FEMHC.

3. Computational details

The molecular geometry deduced from SCXRD data was used as a reasonable initial guess for molecular geometry optimization and this geometry was refined further by optimizing it with the latest PM7 semi-empirical method. The resulting geometry was used as an input geometry for further MP2 *ab initio* calculations. Dunning's correlation consistent triple zeta cc-pVTZ basis set was used for quantum chemical calculations. For reducing the computation time in MP2 calculations the resolution of identity (density fitting) method with an approximation for Coulomb integrals and chain of spheres exchange (RIJCOSX) approximation[36] was used for geometry optimization and frequency calculations. The similar procedure was followed for optimization of the tautomeric transition state. We confirmed that there is no imaginary frequency present in frequencies calculations for MP2 optimized geometries of thione and thiol tautomeric forms. ORCA computational chemistry package version 3.0.3[37] was used to perform MP2 calculations. The MOPAC 2016 program was used for semi-empirical geometry optimization. Input files were written with the help of Gabedit graphical user interface version 2.4.8.[38] Gabedit was also used for post-quantum chemical calculation result parsing, properties calculation, visualization and interpretation of the results. The theoretical assignment of the calculated wavenumbers was done with vibrational animation utility of Jmol Java molecular viewer and Gabedit GUI. The 3D Hirshfeld surfaces plot and 2D-fingerprint plot of FEMHC crystal were obtained using CrystalExplorer software.

RESULTS AND DISCUSSION

1. Crystal data and structure determination

Single crystal X-ray diffraction was performed on a crystal having dimensions of 0.30 × 0.20 × 0.20 mm^3 with graphite monochromatic MoKα radiation (λ = 0.71073Å). The diffraction data were collected at 296 K. The final unit cell was determined from 8955 reflections in the range of 1.28° to 28.34°. The crystal structure has been solved in the triclinic system, space group P-1. Multi-scan absorption correction technique[39] was applied (absorption coefficient μ = 0.274 mm^{-1}) and the maximum and minimum transmission factors were 0.9472 and 0.9223. The structure was solved by direct methods and refined by full-matrix least squares based on F^2 with weight $w = 1/[\sigma^2(F_o^2) + (0.1001P)^2 + 0.2955P]$ where $P = (F_o^2 + 2F_c^2)/3$. The least-squares refinement and difference Fourier calculations revealed the positions of non-hydrogen atoms. The calculation at this point, by PLATON, showed that there was no missed crystallographic symmetry. Non-hydrogen atoms were refined with independent anisotropic displacement parameters. APEX2 software program was used for data collection,[40] APEX2/SAINT program was used for cell refinement,[40,41] SAINT/XPREP program was used for data reduction,[41,42] SIR92 program was used for structure solution,[43] SHELXL-97 program was used for structure refinement, ORTEP-3,[44] Mercury[45] and SHELXL-97 programs were used for molecular graphics and prepare material for publication. The crystallographic data and some details of the structural refinement are summarized in Table 1.

The color code of atoms, asymmetric unit, unit cell and crystal packing of FEMHC crystal are shown in Figure 1. The asymmetric unit contains two slightly different molecular geometries of FEMHC. They are designated as molecule (a) and molecule (b). The geometry of molecule (b) is comparatively more planar than the geometry of molecule (a). The 3D Hirshfeld surface plots and 2D fingerprint show that these two molecules in the asymmetric unit have different chemical environment.

Table 1

Crystal data and structure refinement for FEMHC

Empirical formula	$C_{20}H_{24}F_2N_6S_2$
Formula weight	450.57
Temperature	296(2) K
Wavelength	0.71073 Å
Crystal system	Triclinic
Space group	P-1
Unit cell dimensions	a = 5.7538(6) Å b = 12.3250(15) Å c = 16.4854(15) Å α = 74.248(5)° β = 88.063(5)° γ = 82.940(5)°
Volume	1116.6(2) $Å^3$
Z, Calculated density	2, 1.340 Mg/m^3
Absorption coefficient	0.274 mm^{-1}
F(000)	472
Crystal size	0.30 x 0.20 x 0.20 mm
Theta range for data collection	1.28 to 28.34°
Limiting indices	$7 \le h \le 7$, $-16 \le k \le 16$, $-20 \le l \le 21$
Reflections collected	8955
Independent reflections	5007 [R_{int} = 0.0180]
Completeness to theta = 28.34	89.6%
Absorption correction	Semi-empirical from equivalents
Max. and min. transmission	0.9472 and 0.9223
Refinement method	Full-matrix least-squares on F^2
Data / restraints / parameters	5007 / 0 / 291
Goodness-of-fit on F^2	0.968
Final R indices [$I > 2\sigma(I)$]	R1 = 0.0476, wR2 = 0.1357
R indices (all data)	R1 = 0.0678, wR2 = 0.1625
Largest diff. peak and hole	0.301 and -0.327 e. A^{-3}

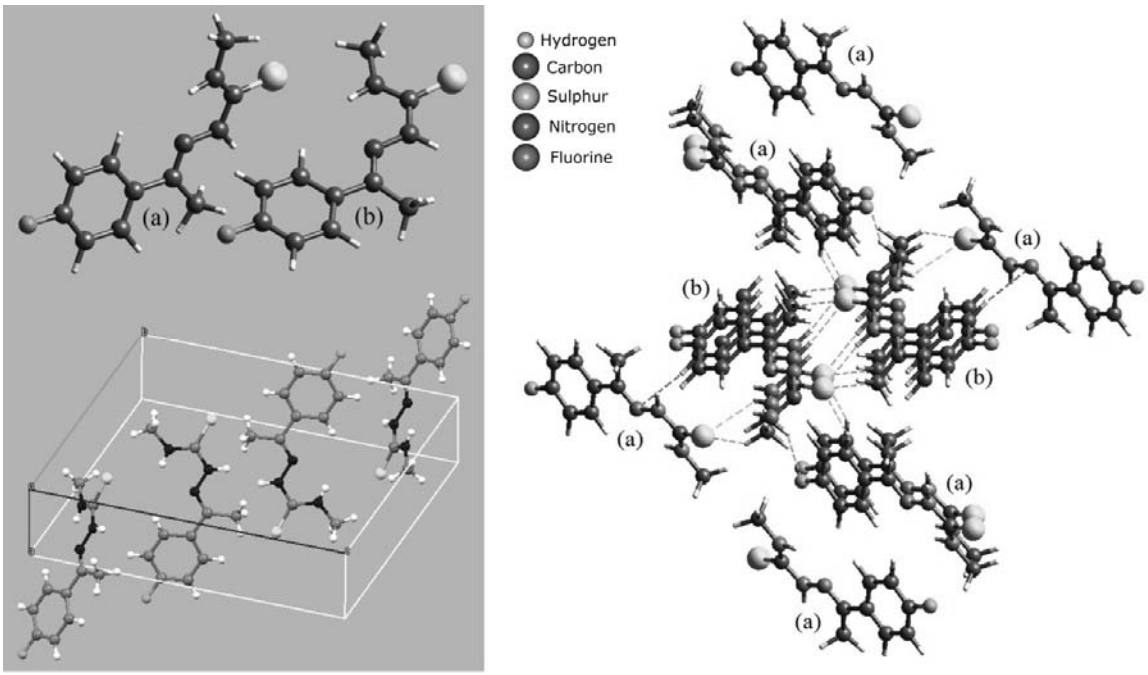

Fig. 1 – Colour code of atoms, asymmetric unit, unit cell and crystal packing with molecular interaction present in the FEMHC crystal. The yellow dashed line show S….H interaction, the green dashed line show F….H interaction and the blue dashed line show N….H interaction.

The close contact interactions are also shown in the Figure 1. The corresponding geometrical parameters are given in Table 2.

The H….A distance and D-H….A angle geometrical considerations infer that N(b)-H….S(b) and C(b)-H….S(b) are comparatively more stronger than of close contact interactions. The next important close contact interaction is C(b)-H….S(a). These interactions are supposed to contribute relatively more towards crystal binding.

Table 2

Geometrical parameters for intermolecular interactions in FEMHC crystal

D-H….A	D-H (Å)	H….A (Å)	D-H….A angle (^{0})
N(b)-H....S(a)	1.009	2.818 (2.89)	133.63
N(b)-H....S(b)	1.009	2.558 (2.89)	168.67
C(b)-H....F(a)	1.083	2.410 (2.56)	132.79
C(b)-H....N(a)	1.083	2.632 (2.64)	157.64
C(b)-H....S(b)	1.083	2.492 (2.89)	149.28
C(b)-H....S(a)	1.083	2.616 (2.89)	137.25
C(a)-H....S(b)	1.083	2.841 (2.89)	153.40

2. Hirshfeld surfaces analysis

The molecular Hirshfeld surface (HS) is a 3D surface in space where the electron density contribution of spherical atoms of a molecule equals the contribution from the rest of the crystal. The Hirshfeld surface mapped with different variables can give valuable chemical information about close contacts and intermolecular interactions. The most important mapping variable for Hirshfeld surface is d*norm* distance which is a normalized contact distance expressed as follows –

$$\mathrm{d}norm = \frac{\mathrm{d}_i - \mathrm{r}_i^{vdw}}{\mathrm{r}_i^{vdw}} + \frac{\mathrm{d}_e - \mathrm{r}_e^{vdw}}{\mathrm{r}_e^{vdw}}$$

where d*i* is the distance to the nearest nucleus internal to the surface, d*e* is the distance to the nearest nucleus external to the surface and r represents corresponding van der Waals (vdW) radii of the atoms. The d*norm* value may be negative or positive depending on whether intermolecular contacts are shorter or longer than van der Waals separations. Where in the space the Hirshfeld surfaces of the two nearby molecules touch each other, they show an identical red spot of the same size, color, and intensity. The d*norm* mapped Hirshfeld surfaces provide identification of the regions of intermolecular interactions and serve as a robust qualitative and quantitative investigation tool for a deeper insight into the intermolecular interaction study of molecular crystals. The CrystalExplorer program uses a red-blue-white color scheme for mapping d*norm* values onto Hirshfeld surface. The red colored regions correspond to close contacts and negative d*norm* value, the white colored regions correspond to the contacts equalizing van der Waals distances with a zero d*norm* value and the blue colored regions correspond to longer contacts and positive d*norm* value. The d*i* versus d*e* two dimensional plot provides facile assignment of an intermolecular contact with a certain type of interaction and provides a complete quantitative summary of the nature and type of intermolecular contacts in a crystal. They are unique plots for a crystal and termed as 2D fingerprint plots. The immediate surrounding environment of a molecule could be studied in terms of the intermolecular interactions in a crystal. Other important properties based on the local curvature of the surface the shape index and the curvedness when mapped on Hirshfeld surfaces give important information about complementary hollows, bumps and coordination number of a molecule respectively. The Hirshfeld surface analysis reveals the strength and role of the strong intermolecular interactions like hydrogen bonds and other non-covalent intermolecular contacts in the crystal lattice, crystal stability, and their relative importance.

The mapped semi-transparent 3D Hirshfeld surfaces of FEMHC molecules (a) and (b) are shown in Figure 2 and 4 respectively. The corresponding 2D fingerprint plots are shown in Figure 3 and 5 respectively.

In Figure 2, the d*norm* mapped Hirshfeld surfaces (2-i) show point of close contact as red color spots. The biggest red spot on right hand side corresponds to C(b)-H….S(a) interaction. The adjacent red spot corresponds to N(b)-H….S(a) interaction and the red spot at left hand side of (2-i) plot show C(b)-H….F(a) interaction. These interactions are visible in d*e* plot (2-iv) as red and orange spots. The d*e* mapped HS shows a large orange colored depression directly above the aromatic ring. The shape index mapped HS also show a red spot directly above the aromatic ring and the curvedness mapped HS show a blue green colored flat area of low curvedness above this aromatic ring. All these features collectively indicate the presence of CH….π interaction for FEMHC (a) molecule in the crystal. The presence of wings feature in 2D fingerprint plot of C….H interaction clearly shows presence of CH….π interaction for FEMHC (a) molecule (Figure 3).

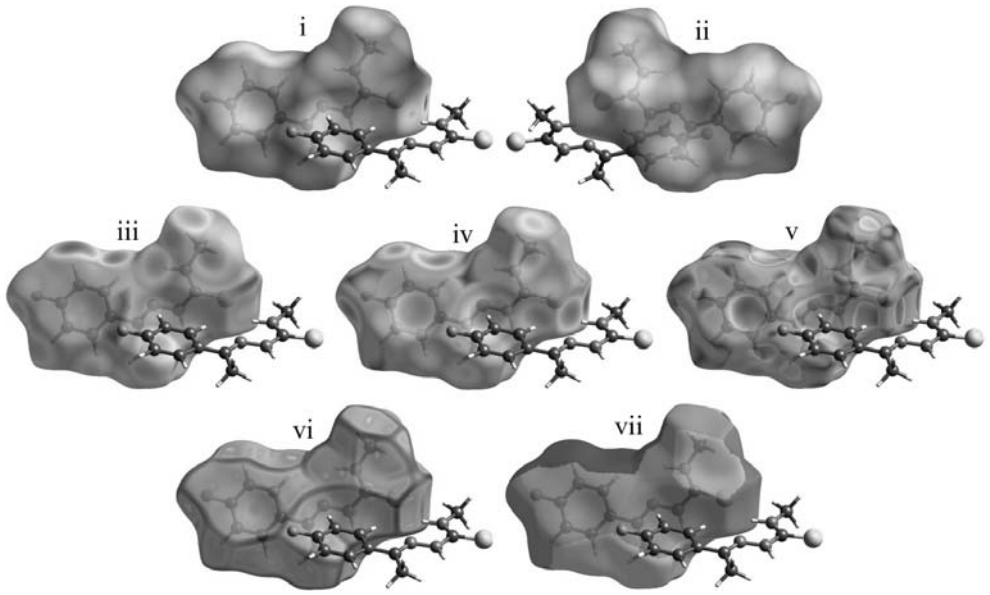

Fig. 2 – The 3D Hirshfeld surface for the FEMHC (a) molecule mapped with (i) d*norm* front view (ii) d*norm* back view (iii) di (iv) de (v) shape-index (vi) curvedness and (vii) Fragment patches.

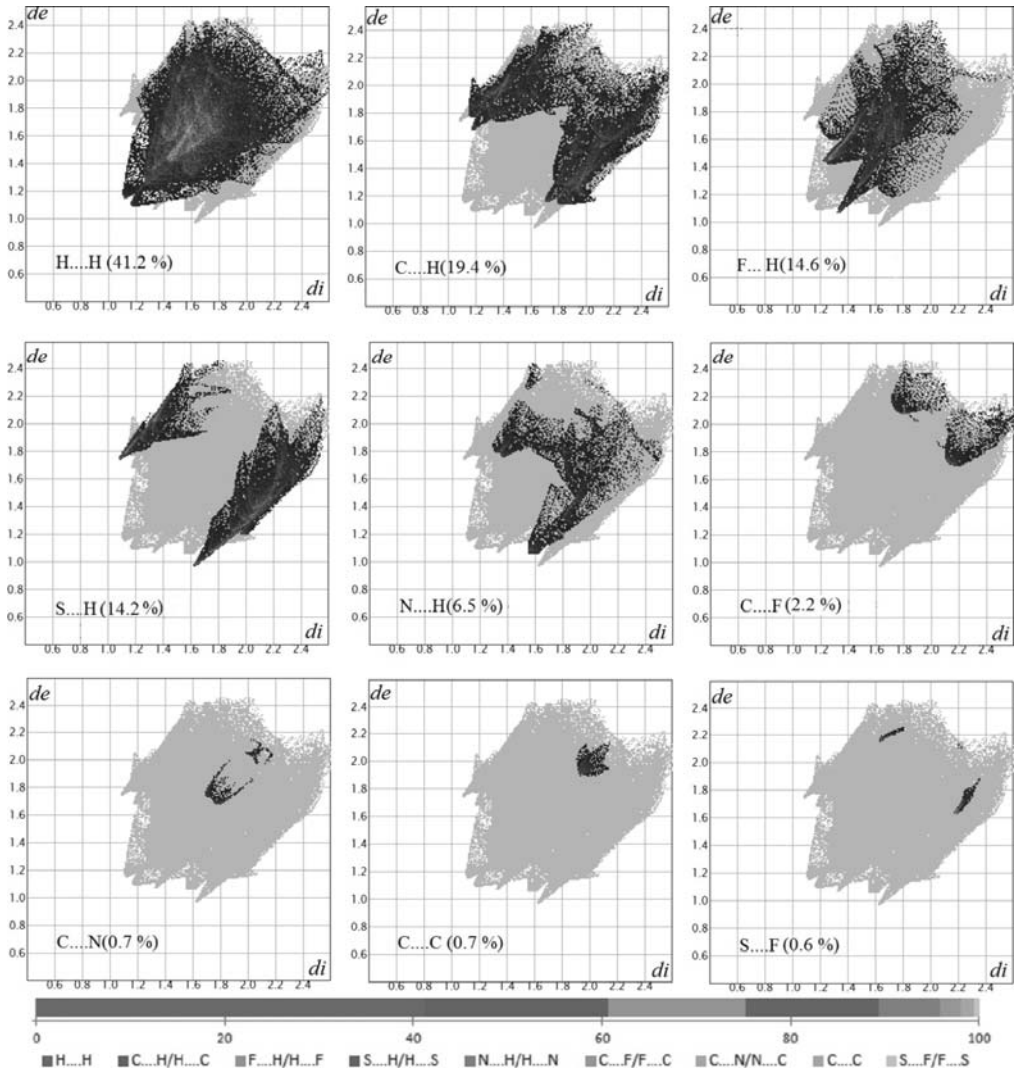

Fig. 3 – The resolved 2D fingerprint to show the percentages of contacts contributed to the total Hirshfeld surface area of the molecule (a) for different intermolecular interactions within the FEMHC crystal.

The 2D fingerprint plots of Hirshfeld surface for molecule (a) reveals that the most important intermolecular contacts for FEMHC (a) molecule in the crystal is H….H contacts. The H….H interaction for FEMHC (a) molecule contributes a total of 41.2% to the HS area of FEMHC (a) molecule. The other main intermolecular interactions for FEMHC molecule (a) in the crystal are C….H, F….H, S….H intermolecular interactions with the relative contribution of each type of contact as 19.4%, 14.6%, and 14.2% respectively. Low percentage contacts are observed for the N….H (6.5%), C….F (2.2%), C….N (0.7%), C….C (0.7%), and S….F (0.6%) contacts.

The resolved 2 D fingerprint plot for H…H interaction show the closest contact at d$e \simeq$ d$i \simeq$ 1.15 Å distance. The H….H interaction plot show splitting at the nose portion, indicative of three-atom closest contact instead of direct contact between two atoms. The next important interaction in FEMHC crystal for molecule (a), the C….H interaction show the closest contact at d$e \simeq$ 1.68 Å and d$i \simeq$ 1.16 Å. The wings type distinct features are also visible on both the flanks of the resolved 2 D fingerprint plot for C….H interaction. This feature clearly indicates the presence of C-H….π interactions for FEMHC (a) molecule. The third important interaction in FEMHC crystal for molecule (a) is F….H interaction with closest contact as acceptor at d$e \simeq$ 1.07 Å and d$i \simeq$ 1.34 Å distance. This F….H interaction is C-H….F type and it is visible as green dashed line in the crystal packing diagram (Figure 1). The fourth important interaction is S….H interaction which shows corresponding two spikes. The closest contact lay on acceptor side at d$e \simeq$ 0.97 Å and d$i \simeq$ 1.64 Å distances. The close S….H acceptor contact interactions are C-H….S and N-H….S type whereas the closest S….H donor contact interaction is C-H….S type only (Figure 1). The N….H interaction for FEMHC (a) molecule contributes only 6.5 % of HS area. The closest N….H acceptor contact interaction is N….H-C(b) type (Figure 1). The N….H interaction shows closest contact on acceptor side at d$e \simeq$ 1.54 Å and d$i \simeq$ 1.06 Å distance.

In Figure 4 at the d*norm* mapped HS, the large circular deep red depressions indicate hydrogen bonding like contacts. The d*norm* mapped surface (Fig. 4-i) show presence of S….H and N….H close hydrogen bond like interactions for FEMHC (b) molecule in the crystal. The most important feature shown by shape index mapped HS plot (v) is the presence of adjacent red and blue triangle oblate just above the aromatic ring, which indicates that the FEMHC (b) geometry in the crystal has significant π….π stacking interaction. The curvedness and fragment patch mapping of HS (Fig. 4-vi and vii) plots of FEMHC (b) molecule show same area slightly oblate above aromatic ring. These features collectively confirm the presence of π….π stacking interaction for FEMHC (b) molecule in the crystal. The small triangular blue regions of convex curvature visible over C(b)-H and N(b)-H hydrogen atoms confirm the presence of hydrogen bond donor like sites and the small triangular red regions of concave curvature visible over S atom visible in shape index mapped confirms the presence of hydrogen bond acceptor like site in FEMHC (b) molecule. The curvedness mapped on the HS plot (4-vi) shows both larger and smaller regions of low curvedness.

The 2D fingerprint plots of Hirshfeld surface for FEMHC (b) molecule reveals that the most important intermolecular contacts for this molecule in the crystal is H….H contacts. The H….H interaction for FEMHC (b) molecule contributes a total of 38.9% to the HS area. The other main intermolecular interactions for FEMHC molecule (b) in the crystal are S….H, F….H and C….H intermolecular interactions with the relative contribution of each type of contact as 18.0%, 13.8%, and 13.3% respectively. Low percentages are observed for the N….H (5.3%), C….N (4.3%), C….C (3.6%), N….S (1.4%), S….C (0.8%) and C….F (0.6%) contacts.

The H…H interaction 2 D plot show the closest contact at d$e \simeq$ d$i \simeq$ 1.26 Å distance. The H….H interaction plot show splitting at the nose portion, indicative of three-atom closest contact feature. The next important intermolecular interaction for FEMHC (b) molecule in the crystal, the S….H interaction show two distinct spikes in the left bottom corner of the plot having the closest contact on acceptor side at d$e \simeq$ 0.94 Å and d$i \simeq$ 1.55 Å. The S….H donor interaction is C-H….S and N-H….S type (Figure 1). The third important interaction in FEMHC crystal for molecule (b) is F….H interaction with the closest contact as a donor at d$e \simeq$ 1.33 Å and d$i \simeq$ 1.08 Å distance. The N….H interaction shows closest contact on donor side at d$e \simeq$ 1.54 Å and d$i \simeq$ 1.08 Å distance. This N….H acceptor interaction is N….H-C type and it is visible as blue dashed lines in the crystal packing diagram (Figure 1). The C….C interaction 2D fingerprint plot show a blue green area at the diagonal at de = d$i \simeq$ 1.75 Å

distance. This show the presence of π….π stacking for FEMHC (b) molecule in the crystal. The inter layer distance manifesting π….π stacking interaction is 3.5 Å.

3. Tautomerism

The optimized structural parameters for the thione form of FEMHC (a) molecule were calculated by MP2/cc-pVTZ method. The atom numbering for FEMHC (a) molecule is shown in Figure 6. The regression coefficient for the calculated bond lengths values was found as 0.9648 and for the calculated bond angles values the regression coefficient was found as 0.8341. The maximum difference in bond length values was found for N22-N23 bond (0.0298 Å) and C16-C14 bond (0.0272 Å) followed by C16-C17 bond (0.0262 Å). The maximum difference in bond angle values was found for ∠ C5-N21-C1 (2.405^0) and ∠ N22-C5-N21 (2.268^0) followed by ∠ N22-C5-S25 (1.722^0). In general, the theoretically predicted bond lengths are found in good agreement with experimental X-ray crystal structure data. While comparing the theoretical bond angle values with observed bond angle values, we find that most of the optimized bond angles differ only a little bit from the experimentally observed bond angle values. The differences between experimentally observed and theoretically calculated values for bond angles are due to the fact that experimental values of bond angles are measured in the solid state whereas, the theoretical calculations are performed in gaseous state in absence of any intermolecular interaction. In spite of the differences, the calculated geometric parameters show a good approximation to experimental values and they may serve as a basis for calculating other molecular parameters and they may be used in further study of FEMHC on theoretical ground.

The thiosemicarbazones have a thione group (C=S) with a proton adjacent to it. The thione group (C=S) is relatively unstable in monomeric form and it tends to form a more stable C-S single bond by enethiolization if there is at least one hydrogen atom available adjacent to the thione (C=S) bond.[50] The thiosemicarbazones are generally expected to show thione-thiol tautomerism. This tautomerism is supposed to take place by proton transfer mechanism through a transition state. The IR spectrum of FEMHC does not show υ(S-H) at *ca.* 2570 cm^{-1}. This shows that thione form predominates in the solid state.

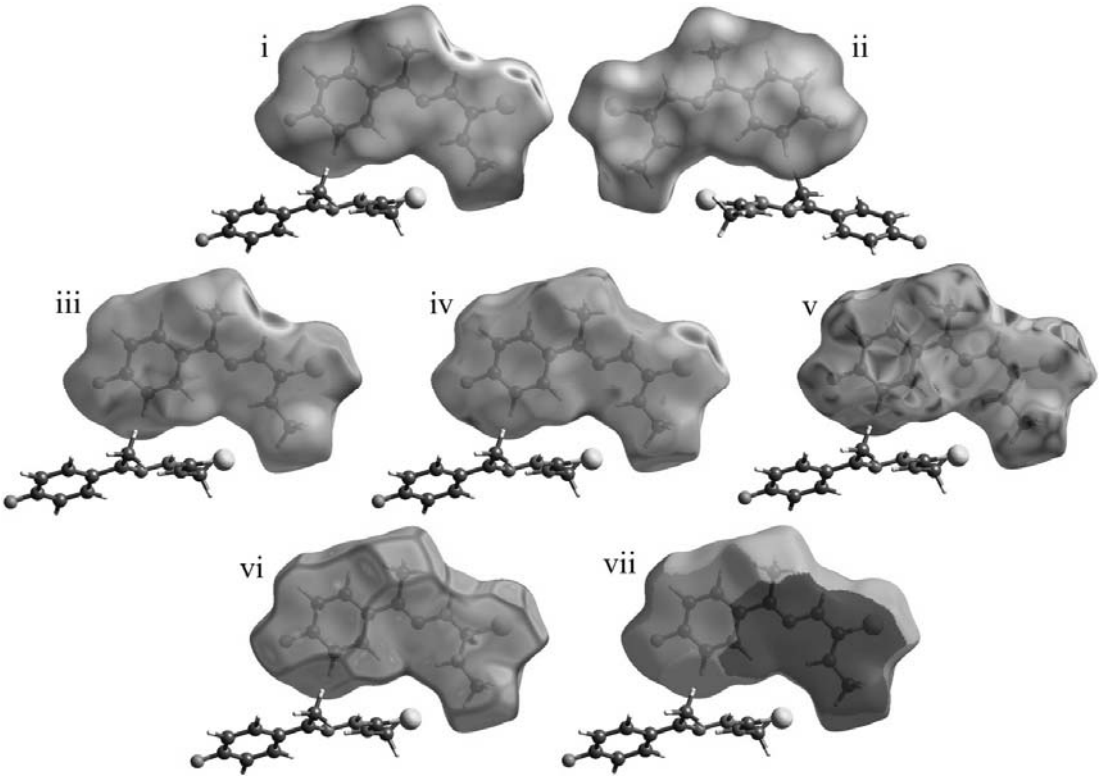

Fig. 4 – The 3D Hirshfeld surface for the FEMHC (b) molecule mapped with (i) d*norm* front view (ii) d*norm* back view (iii) di (iv) de (v) shape-index (vi) curvedness and (vii) Fragment patches.

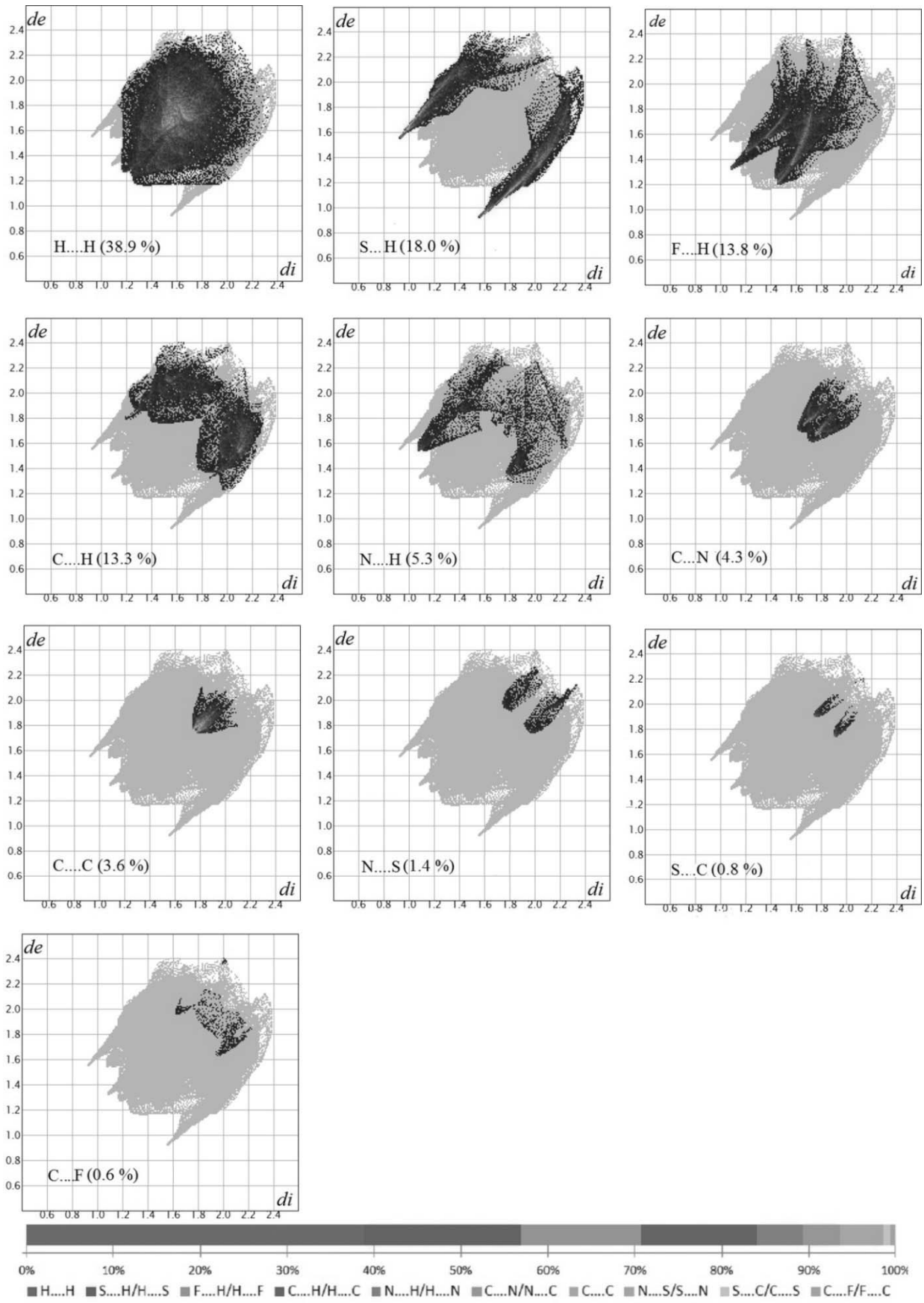

Fig. 5 – The resolved 2D fingerprint to show the percentages of contacts contributed to the total Hirshfeld surface area of the molecule (b) for different intermolecular interactions within the FEMHC crystal.

Exploring relative stabilities of tautomeric forms is important for the molecular structural point of view. To investigate thione-thiol tautomerism theoretically, the thiol tautomeric form and the transition state (TS) of tautomeric conversion were also optimized at the same basis set level by MP2 method. The calculated energy of optimized geometries of thione, intermediate tautomeric conversion TS and thiol form come out as -1048.831932596264 Eh, -1048.782070020374 Eh and -1048.811950663857 Eh respectively. The tautomeric conversion of FEMHC (a) molecule is shown in Figure 6.

The forward energy barrier for tautomerization was calculated as 130.90 kJ/mol and the thione tautomeric form was found more stable than thiol tautomeric form by 52.46 kJ/mol. The theoretical investigation shows that in the thione-thiol transformation the N-H bond length in thione form increases from 1.0114 Å to N….H distance of 1.3376 Å in the transition state and the S….H distance in the transition state is reduced from 1.6356 Å to 1.3376 in S-H bond. The ab initio energy calculation reveals that the expected phenomenon of thione to thiol prototropic tautomerization for FEMHC is not favorable thermodynamically in the gaseous state.

4. Vibration frequencies

The experimentally observed and the calculated scaled IR fundamental vibration frequencies for FEMHC by MP2 method are given in Table 3. The theoretically predicted IR spectrum obtained from the MP2 method does not show any imaginary frequency. The scaling factor used for scaling the calculated vibrational frequencies below 1000 cm^{-1} is 1.0638 and the scaling factor used for scaling calculated vibrational frequencies above 1000 cm^{-1} is 0.9575 for MP2/cc-pVTZ method[47]. The difference between calculated and experimental frequencies is due to anharmonic intermolecular interactions, approximation treatment of electronic correlation effects and the limited basis sets. The calculated frequencies show a nice approximation with experimental frequencies. Only a few discrepancies observed. The probable assignments to experimental frequencies are also given in this table according to reported indications.[48–52]

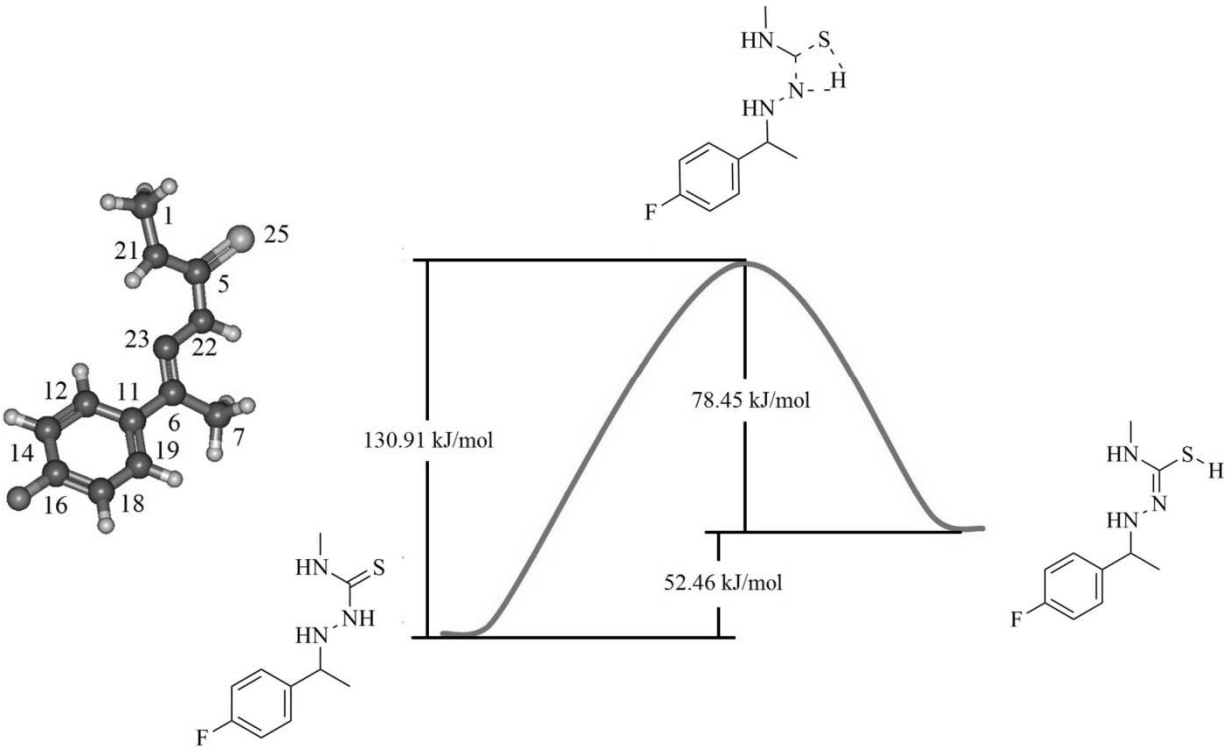

Fig. 6 – Atom numbering of MP2 optimized geometry and tautomerism of FEMHC (a) molecule.

Table 3

Selected vibration frequencies for the thione
form of FEMHC experimentally obtained and the calculated vibration frequencies by MP2/cc-pVTZ method

Experimental vibration frequencies			Calculated vibration frequencies		
Freq.	**Trans. %**	**Assign.**	**Freq.**	**Inten.**	**Assign.**
462.80	21.68	N-H π	490.94	107.36	N22-H π
590.33	57.67	N-H π	542.70	19.11	N21-H π
665.60	56.76	ring δ	614.73	15.78	ring δ
756.33	48.90	ring δ			
811.47	47.89	C=S ν, ring δ	889.64	31.12	C=S ν, ring δ E2g
839.01	39.27	ring C-H π	905.23	65.17	ring C-H π A2u
			958.30	23.16	$-CH_3$ π
			1038.62	54.91	$-CH_3$ π
			1044.37	67.46	$-CH_3$ π
1045.56	39.97	ring C-H β	1070.52	16.76	ring CH β E1u
			1124.81	109.63	ring CH β E2g
1106.77	41.3	N-N ν	1131.39	50.60	N-N ν, ring C-H β
			1152.86	34.94	$-CH_3$ π
1160.28	42.79	C-N ν	1198.45	438.96	C5-N22 ν, N22-H β, $-CH_3$ β
1230.17	26.72	C-F	1223.40	62.16	C-F, ring CH β E1u
1299.11	38.12	C-N ν	1282.08	137.13	N21-H β, N22-H β, C5-N21 ν
1367.36	49.48	N-H β, $-CH_3$ ν	1331.42	31.65	N21-H β, $-CH_3$ β
			1390.72	42.10	$-CH_3$ β
			1429.23	145.87	$-CH_3$ β
1413.93	42.99	$-CH_3$ β	1440.48	167.49	$-CH_3$ β
			1458.83	144.18	$-CH_3$ β, N22-H27 β
1495.44	23.08	N-H β	1463.43	446.11	N21-H26 β, N22-H27 β, $-CH_3$ β
1549.20	22.02	C=N ν	1521.29	65.25	C6=N23 ν
			1522.78	400.83	C5-N21 ν
1602.98	43.01	ring C-C ν	1587.88	108.05	ring C-C ν E2g
2939.68	51.63	$-CH_3$ ν	2947.35	45.21	$-CH_3$ ν_s
3304.14	39.90	N-H ν	3430.64	44.78	N22-H ν
3370.21	41.95	N-H ν	3461.15	111.17	N21-H ν

Freq.: frequency in cm^{-1}, Trans.**:** Transmittance, Assign.: assignment, Inten.: intensity in km/mol, ring: aromatic ring, ν: stretching, β: bending, a: asymmetric, s: symmetric, π: out of the plane bending, δ: deformation.

In the experimental IR spectrum the vibration frequency at 3304.14 cm^{-1} for secondary amine (>N-H) stretch is observed in the expected range and the other vibration frequency at and 3370.21 cm^{-1} falls a little outside (10 cm^{-1}) the suggested range.[52] The vibration frequency observed at 2939.68 cm^{-1} corresponds to methyl stretch. No characteristic vibration frequency for thiol S-H stretch was observed in IR spectrum of this compound. Assigning the vibration absorptions in the middle frequency range is difficult due to strong coupling among different vibrations in this range. The absorption observed at 1602.98 cm^{-1} is assigned to aromatic ring stretch. The secondary amine, NH bending vibration at 1495.44 cm^{-1} is observed approximately 55 cm^{-1} lower than the range of 1650-1550 cm^{-1} as specified by Coates.[52] The monofluorobenzenes show a sharp absorption near 1230 cm^{-1}.[53] The theoretically calculated value for this vibration in the present study is 1223.40 cm^{-1}, so the experimental frequency observed at 1230.17 cm^{-1} is assigned as aromatic C-F vibration. It was inferred earlier that in the thiosemicarbazones, the C=S vibrations may be observed in the uncoupled pure form in the range 830-805 cm^{-1} and in the coupled form they may be observed in the range 1110-1075 cm^{-1}.[50] We assigned 811.47 cm^{-1} C=S stretching vibrations

accordingly. The vibration at 1106.77 cm^{-1} is supposed to have some contribution from C=S stretching vibration. This vibration is expected to be strongly coupled with N-C-N stretching vibration[50] and aromatic ring C-H in plane bending vibration. The theoretical assignment for this vibration is N-N stretching coupled with ring C-H in plane bending vibration.

5. Electron localization function plot

Electron localization function (ELF) was proposed as a simple measure of localization of electron in atomic and molecular systems by Becke and Edgecombe.[54] They defined ELF as follows:

$$0 \leq \mathrm{ELF} \leq 1,$$

where is the difference of kinetic energy density of the non-interacting system and von Weizsäcker kinetic energy density,is the value of term for the homogeneous electron gas.

Savin further generalized ELF approach to a variety of chemical systems.[55] The ELF isosurfaces plots topologically distinguish the type of bonding in a chemical species. The ELF 3D isosurface[56] for FEMHC as calculated by Gabedit for MP2/cc-pVTZ calculation output is shown in Figure 7.

Non-bonding ring attractor domains are visible on F24 and S25 atoms. The non-bonding attractors on N atoms are visible as merged with nearby bonding attractors. The disynaptic basins V(C,C) for aromatic rings show an intermediate shape as shown by a typical C-C single bond and C=C double bond. The V(C,H) disynaptic basins show their typical shape. A single bean shaped V(C,S) disynaptic basin arisen for the C5=S25 bond.

CONCLUSION

(2E)-2-[1-(4-fluorophenyl)ethylidene]-*N*-methyl-hydrazine -1-carbothioamide was synthesized and characterized. The asymmetric unit of FEMHC crystal contains two slightly differ molecular geometries having different chemical environment. The Hirshfeld surface analysis of FEMHC crystal shows the existence of different close contacts. The S….H and F….H close contacts are the major contributing interactions responsible for crystal packing. The Hirshfeld Surface analysis shows presence of the π….π stacking for one type of molecular geometry and presence of the weak C-H….π interactions for the other molecular geometry. Theoretical findings conclude that the thione tautomeric form is thermodynamically more stable than thiol tautomeric form by 52.46 kJ/mol in the gaseous phase. The thione tautomer predominates in the solid state. The ELF isosurface plots show typical localization domains for FEMHC.

Acknowledgements. Rajeev Singh gratefully acknowledges the financial support for this work by the Madhya Pradesh Council of Science and Technology (MPCST), Bhopal by means of Research Grant No. 1076/CST/R&D/2012. Authors thankful to‘Sophisticated Test and Instrumentation Centre, Cochin University of Science and Technology, Cochin - 682 022, Kerala, India’ for carrying out SCXRD experiment. Authors also thankful to ‘Sophisticated Analytical Instrument Facility, CSIR-Central Drug Research Institute, Lucknow-226031, Uttar Pradesh, India’ for carrying out Mass, IR, and NMR spectral experiment

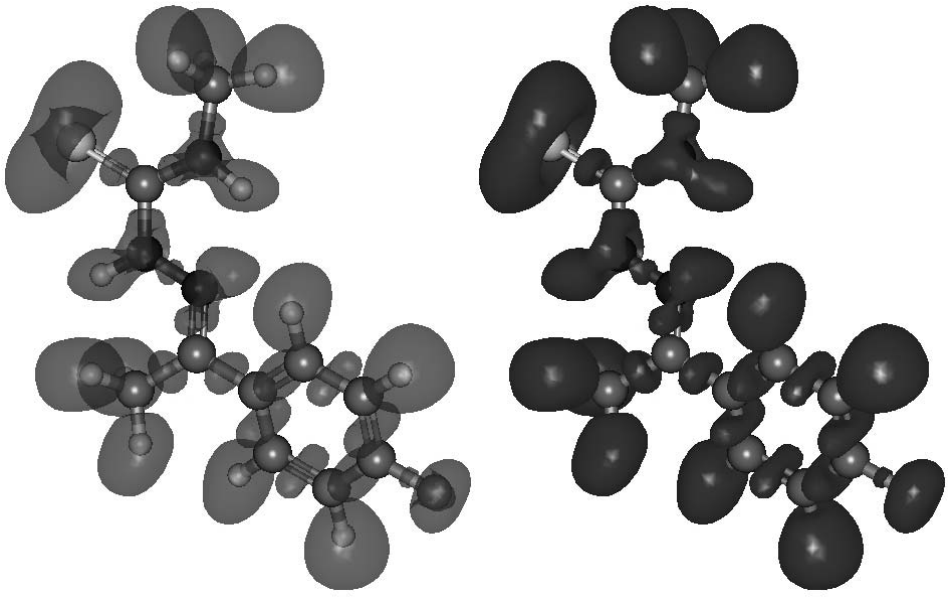

Fig. 7 – ELF of TSC1 thione form at level 0.8.

REFERENCES

1. H. Steinhagen, *Chem. Med. Chem.,* **2011**, *6*, 1746–1747.
2. W. Sneader, "Drug Discovery", John Wiley & Sons Ltd, 2005, Vol. xlv.
3. T. Trnka, in "Antituberculosis Drugs", K. Bartmann (Ed.) Springer Science & Business Media: Berlin Heidelberg, 1988. p 92.
4. A. S. Dobek, D. L. Klayman, E. T. Dickson, J. P. Scovill and E. C. Tramont, *Antimicrob. Agents Chemother.*, **1980**, *18*, 27–36.
5. M. Sheikhy, *J. Biomed. Sci. Eng.,* **2012**, *5*, 39–42.
6. H. Pervez, N. Saira, M. S. Iqbal, M. Yaqub and K. M. Khan, *Molecules,* **2011**, 6408–6421.
7. N. Parul, N. Subhangkar and M. Arun, **2012**, *3*, 350–363.
8. D. M. Wiles and T. Suprunchuk, *J. Med. Chem.*, **1971**, *14*, 252–254.
9. B. A. Gingras, G. Colin and C. H. Bayley, *J. Pharm. Sci.,* **1965**, *54*, 1674–1675.
10. S. Mylonas and A. Mamalis, *J. Heterocycl. Chem.*, **2005**, *42*, 1273–1281.
11. M. C. Liu, T. C.; Lin and A. C. Sartorelli, *J. Med. Chem.* **1992**, *35*, 3672–3677.
12. M. A. Soares, J. A. Lessa, I. C. Mendes, J. G. Da Silva, R. G. Dos Santos, L. B. Salum, H. Daghestani, A. D. Andricopulo, B. W. Day, A. Vogt, J. L. Pesquero, W. R. Rocha and H. Beraldo, *Bioorg. Med. Chem.*, **2012**, *20*, 3396–3409.
13. Y. Wang, M. C. Liu, T. S. Lin and A. C. Sartorelli, *J. Med. Chem.,* **1992**, *35*, 3667–3671.
14. A. Matesanz and P. Souza, *Mini Rev. Med. Chem.*, **2009**, *9*, 1389–1396.
15. K. C. Agrawal, P. D. Mooney and A. C. Sartorelli, *J. Med. Chem.,* **1976**, *19*, 970–972.
16. K. C. Agrawal, B. A. Booth, S. M. DeNuzzo and A. C. Sartorelli, *J. Med. Chem.,* **1976**, *19*, 1209–1214.
17. B. Prescott and C. Pein Li, *J. Med. Chem.,* **1964**, *7*, 383–385.
18. P. V. S. Naidu, P. Kinthada and Y. L. N. Murthy, *Int. J. Pharm.,* **2011**, *2*, 92–98.
19. D. S. Kalinowski, P. Quach and D. R. Richardson, *Future Med. Chem.,* **2009**, *1*, 1143–1151.
20. U. Kulandaivelu, V. G. Padmini, K. Suneetha, B. Shireesha, J. V. Vidyasagar, T. R. Rao, A. Basu and V. Jayaprakash, *Arch. Pharm. (Weinheim),* **2011**, *344*, 84–90.
21. S. Arora, S. Agarwal and S. Singhal, *Int. J. Pharm. Pharmaceutical Sci.,* **2014**, 34–41.
22. W. Hu, W. Zhou, C. Xia and X. Wen, *Bioorg. Med. Chem. Lett.,* **2006**, *16*, 2213–2218.
23. V. C. Barry, M. L. Conalty and J. F. O'Sullivan, *Cancer Res,.* **1966**, *26*, 2165–2168.
24. H. D. Patel and S. A. Shah, *Der Pharm. Sin.,* **2012**, *3*, 199–210.
25. R. Pingaew, S. Prachayasittikul and S. Ruchirawat, *Molecules,* **2010**, 988–996.
26. D. L. Klayman, A. J. Lin, J. W. McCall, S. Y. Wang, S. Townson, M. Grögl and K. E. Kinnamon, *J. Med. Chem.,* **1991**, *34*, 1422–1425.
27. C. Shipman, S. H. Smith, J. C. Drach and D. L. Klayman, *Antimicrob. Agents Chemother.,* **1981**, *19,* 682–685.
28. D. J. BAUER, P. W. SADLER and P. W. S. BAUER, *Br. J. Pharmacol. Chemother.,* **1960**, *15*, 101–110.
29. R. POLLIKOFF, M. LIEBERMAN, N. E. LEM and E. J. FOLEY, *J. Immunol.,* **1965**, *94*, 794–804.
30. Y. V. Patskovsky, E. N. Negrebetskaya, A. A.Chernomaz, T. P. Voloshchuk, E. L. Rubashevsky, O. E. Kitam, M. I. Tereshchenko, L. N. Nosach and A. I. Potopalsky, *Biopolym. Cell,* **1996**, *12*, 74–83.
31. J. Easmon, G. Heinisch, W. Holzer and B. Rosenwirth, *Arzneimittelforschung.,* **1989**, *39*, 1196–1201.
32. R. Slack, K. R. H. Wooldridge, J. A. McFadzean and S. Squires, *Nature* **1964**, *204*, 587–587.
33. L. Sebastian, A. Desai, M. N. Shampur, Y. Perumal, D. Sriram and R. Vasanthapuram, *Virol. J.,* **2008**, *5*, 64–71.
34. P. Padmanabhan, S. Khaleefathullah, K. Kaveri, G. Palani, G. Ramanathan, S. Thennarasu, U. Tirichurapalli Sivagnanam, *J. Med. Virol.,* **2017**, *89*, 546–552.
35. B. Jaroszynska-weinberger, B. Jaroszyńska-Weinberger and B. Jaroszynska-weinberger, *Arch. Dis. Child.,* **1970**, *45*, 573–580.
36. S. Kossmann and F. Neese, *J. Chem. Theory Comput.,* **2010**, *6*, 2325–2338.
37. F. Neese, *Wiley Interdiscip. Rev. Comput. Mol. Sci.,* **2012**, *2*, 73–78.
38. S. K. Wolff, D. J. Grimwood, J. J.; McKinnon, M. J.; Turner, D. Jayatilaka and M. A. Spackman, ????,2012.
39. Bruker (1999). Bruker AXS Inc.: Madison, Wisconsin, USA. 1999.
40. Bruker (2004). Bruker AXS Inc.: Madison, Wisconsin, USA. 2004.
41. Bruker (2004). Bruker AXS Inc.: Madison, Wisconsin, USA. 2004.
42. Bruker (2004). Bruker AXS Inc.: Madison, Wisconsin, USA. 2004.
43. A. Altomare, G. Cascarano, C. Giacovazzo and A. Guagliardi, *J. Appl. Crystallogr.,* **1993**, *26*, 343–350.
44. L. J. Farrugia, *J. Appl. Crystallogr.* **1997**, *30*, 565–565.
45. C. F. Macrae, P. R. Edgington, P. McCabe, E. Pidcock, G. P. Shields, R. Taylor, M. Towler, J. van de Streek, *J. Appl. Crystallogr.,* **2006**, *39*, 453–457.
46. R. Mayer, in "Organosulfur chemistry", M. J. Janssen (Ed.), Interscience, New York: New York, 1967, p. 17.
47. P. Sinha, S. E. Boesch, C. Gu, R. A. Wheeler, A. K. Wilson, *J. Phys. Chem. A,* **2004**, *108*, 9213–9217.
48. C. N. R. Rao and R. Venkataraghavan, *Spectrochim. Acta,* **1962**, *18*, 541–547.
49. D. M. Wiles and T. Suprunchuk, *Can. J. Chem.,* **1969**, *47*, 1087–1089.
50. D. M. Wiles, B. A. Gingras, T. Suprunchuk and B. A. Gingkas, *Can. J. Chem.,* **1967**, *45*, 469–473.
51. C. N. R. Rao, R. Venkataraghavan and T. R. Kasturi, *Can. J. Chem.,* **1964**, *42*, 36–42.
52. J. Coates, in "Encyclopedia of Analytical Chemistry", 2000, p. 10815–10837.
53. D. N. Sathyanarayana, "Vibrational spectroscopy□: theory and applications", New Age International, 2004.
54. A. D. Becke and K. E. Edgecombe, *J. Chem. Phys.,* **1990**, *92*, 5397.
55. A. Savin, R.Nesper, S. Wengert and T. F. Fässler, *Angew. Chemie Int. Ed. English,* **1997**, *36*, 1808–1832.
56. A. Savin, B. Silvi and F. Colonna, *Can. J. Chem.,* **1996**, *74*, 1088–1096.